

Gravitational waves from tidal disruption events: an open and comprehensive catalogue

Martina Toscani,^{1,2*} Giuseppe Lodato¹, Daniel J. Price³ and David Liptai³

¹ *Dipartimento di Fisica, Università Degli Studi di Milano, Via Celoria, 16, Milano, 20133, Italy*

² *Laboratoire des 2 Infinis - Toulouse (L2IT-IN2P3), Université de Toulouse, CNRS, UPS, F-31062 Toulouse Cedex 9, France*

³ *School of Physics and Astronomy, Monash University, Clayton Vic 3800, Australia*

Accepted XXX. Received YYY; in original form ZZZ

ABSTRACT

We present an online, open and comprehensive template library of gravitational waveforms produced during the tidal disruptions of stars by massive black holes, spanning a broad space of parameters. We build this library thanks to a new feature that we implement in the general relativistic version of PHANTOM, a smoothed particle hydrodynamics code for three dimensional simulations in general relativity. We first perform a series of numerical tests to show that the gravitational wave (GW) signal obtained is in excellent agreement with the one expected from theory. This benchmark is done for well studied scenarios (such as binary stellar systems). We then apply our code to calculate the GW signals from tidal disruption events (TDEs), finding that our results are consistent with the theoretical estimates obtained in previous studies for selected parameters. We illustrate interesting results from the catalogue, where we stress how the gravitational signal is affected by variations of some parameters (like black hole spin, stellar orbital eccentricity and inclination). The full catalogue is available online. It is intended to be a living catalogue.

Key words: gravitational waves – hydrodynamics – methods: numerical – black hole physics – accretion, accretion discs

1 INTRODUCTION

Simultaneous detection of the neutron star merger in 2017, both in gravitational waves (GWs, Abbott et al. 2017) and electromagnetic (EM) radiation (Goldstein et al. 2017), has paved the way to an era of multi-messenger astronomy. In the near future, a new generation of interferometers, including LISA (Amaro-Seoane et al. 2017), TianQin (Luo et al. 2016) and DECIGO (Sato et al. 2017), will be launched in space to reveal the low-frequency (10^{-4} – 10^{-2} Hz) GW sky for the first time. At the same time, powerful telescopes, such as Athena (Barcons et al. 2012), Lynx (Gaskin et al. 2018) and LSST (Abell et al. 2009), will search the sky looking for EM counterparts of these gravitational sources.

Among the systems we expect to detect in both domains are stars tidally disrupted by black holes (BHs). Tidal disruption events (TDEs; Rees 1988, Phinney 1989) have been extensively investigated over the last decades both analytically (see the review by Rossi et al. 2020 and references therein) and numerically (see the review by Lodato et al. 2020 and references therein). To date, around 50 events of this type have been seen, in different bands of the EM spectrum (optical: van Velzen et al. 2020, X-ray: Saxton et al. 2020, radio: Alexander et al. 2020). They are characterized by luminous

flares, often super-Eddington, that arise when the stellar debris falls back to the pericenter, typically several days after the star is torn apart by the BH tides.

As for the destruction itself, so far we have not been able to observe it since there is little EM production during that phase. Yet, a star undergoing the disruption emits a GW burst. For a standard scenario of a Sun-like star disrupted by a $10^6 M_{\odot}$ BH, we expect the GW signal to be $\approx 10^{-22}$, with a frequency $\approx 10^{-4}$ Hz (see, e.g., Kobayashi et al. 2004, Toscani et al. 2019). Thus, the frequency is in the right interval for space-based interferometers. Still, the signal is not very strong and for this reason we do not expect LISA to see many events of this type (between zero and a few tens during the whole mission, a quantity *strongly* dependent on the noise sensitivity of the instruments; see Pfister et al. 2021). Contrarily, the post-LISA generation of interferometers (e.g. DECIGO) will be more sensitive and thousands of TDEs will be seen in GWs (Pfister et al. 2021). Hence it is certain that in the future we will have the proper instruments to see the GW emission from TDEs.

For this reason, it is important to have a code that not only can predict the GW emission from a source, but also manages to reproduce the fluid-dynamics accurately. Smoothed particle hydrodynamics (SPH) (Gingold & Monaghan 1977, Lucy 1977, Rosswog 2009, Price 2012) is perfect for this goal. Yet, since we are also interested in gravitational emission, that typically involves compact

* E-mail: martina.toscani@unimi.it

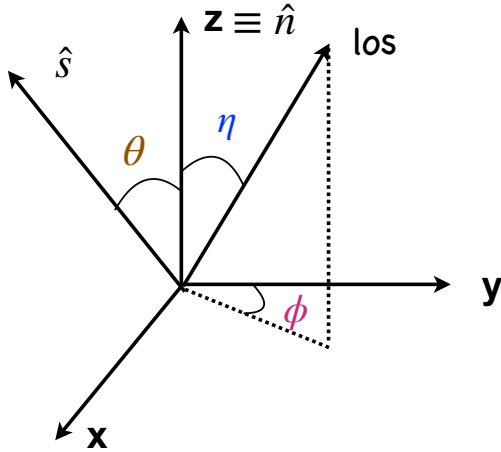


Figure 1. Relations between the $(\mathbf{x}, \mathbf{y}, \mathbf{z})$ frame and the angles η , ϕ , θ . For our TDEs, the stellar orbit lies in the $\mathbf{x} - \mathbf{y}$ plane, the normal to the orbit \hat{n} is along the \mathbf{z} direction. η is the angle between the line of sight (los) and the normal to the orbit, ϕ is the angle among the projection of the los on the $\mathbf{x} - \mathbf{y}$ plane and the pericenter of the star. θ is the angle between the spin of the BH and the normal to the orbit (see Section 4).

objects in strong gravity, we need an SPH code with general relativistic features. A code that couples general relativity (GR) and hydrodynamics is GRPHANTOM (Liptai & Price 2019), the latest version of the PHANTOM code (Price et al. 2018). GRPHANTOM works in any fixed metric (Minkowski, Schwarzschild and Kerr in Cartesian Boyer-Lindquist coordinates), with a proper treatment of orbital dynamics and with the ability to capture relativistic shocks. It is open source and easily available for everyone.

Here we describe our implementation of a module¹ to compute the GW emission in GRPHANTOM and use it to create a library of TDE waveforms. In Section 2 we describe the method, while in section 3 we present standardised test. In Section 4 we discuss the basics of TDE physics and we apply the tool to derive the GW signal produced by the standard scenario of this kind of event. Furthermore, we also show how the GW catalogue has been built (available at this website <https://gwcataloguetdes.fisica.unimi.it>). Finally, we discuss some interesting results in Section 5 and we draw our conclusions in Section 6.

2 METHOD

Assuming the weak field approximation and the Lorenz gauge, the gravitational wave emission is described by (see, e.g., Einstein 1918, Buonanno 2007 and Toscani et al. 2019)

$$h_{ij}^{\text{TT}}(t, \mathbf{x}) = \frac{2G}{dc^4} \Lambda_{ij,kl} \ddot{M}^{kl}(t, \mathbf{x}), \quad (1)$$

where h_{ij}^{TT} is a small perturbation of the background metric (for the TDEs presented here, we use the Kerr metric), G is the gravitational constant, c is the speed of light, d is the distance of the source with respect to the observer, $\Lambda_{ij,kl}$ is the TT operator² and \ddot{M}^{kl} is the second time derivative of the moment of inertia of the system

$$M^{kl} = \int d^3x \rho(t, \mathbf{x}) x^k x^l. \quad (2)$$

¹ It will be soon freely available within GRPHANTOM.

² The superscript TT means that the Transverse Traceless gauge holds.

The index k and l run from 1 to 3 and stand for the spatial coordinates.

Only two components of h_{ij}^{TT} are independent. These components are the *cross polarization* h_{\times} , and the *plus polarization*, h_{+} . If we consider the GW propagating along a generic direction \mathbf{k} , the quadrupole radiation will depend on two angles (see, e.g., Maggiore 2007). Here, we call these angles η and ϕ . We define η as the angle between the line of sight and the \mathbf{z} direction, that we will always consider to be perpendicular to the stellar orbit in our TDE calculations³. Instead ϕ is the angle between the projection of the line of sight on the orbital plane and the \mathbf{y} axis, along which we will always assume the stellar pericenter to lie. These angles are illustrated in Figure 1, where we show also a third angle, θ , that we define later in the paper (cf. Section 4).

Note that, in the rest of the paper, we will call *face-on* polarization amplitudes

$$h_{+} = \frac{G}{dc^4} (\ddot{M}_{11} - \ddot{M}_{22}), \quad (3)$$

$$h_{\times} = \frac{2G}{dc^4} \ddot{M}_{12}, \quad (4)$$

the specific case where the line of sight is along the \mathbf{z} direction and thus $\eta = 0$ (cf. Maggiore 2007).

Since in GRPHANTOM we simulate astrophysical objects as an ensemble of SPH particles, the starting point to implement the calculation of the gravitational emission is to discretize formula (2). We proceed in the following way

$$M^{kl} = \int d^3x \rho(t, \mathbf{x}) x^k x^l \rightarrow \int dm x^k x^l \simeq \sum_b m_b x_b^k x_b^l, \quad (5)$$

where in the last step we have introduced the index b that counts the number of particles. Note that the positions are with respect to the origin of the coordinate system. Starting from this formula, we can compute the second time derivative as

$$\ddot{M}^{kl} = \sum_b m_b (a_l x_k + 2v_l v_k + x_l a_k), \quad (6)$$

where v and a are the velocity and acceleration of the SPH particle. The code knows v and a at each timestep and consequently we can calculate *on the fly* the relevant quantities for the GW emissions: \ddot{M}^{kl} and the polarization amplitudes h_{+} and h_{\times} (for selected values of η and ϕ , see Section 4). Each of these quantities is written in an output file at each time. The acceleration a is computed as the time derivative of the momentum per unit mass, that in GR is in general different from the time derivative of the velocity. Yet, we prefer to use this quantity, that is the acceleration term calculated in the code, since it is the best way to take into account GR effects. In any case, since in our calculation we do not consider ultra-close TDEs, these effects will not be particularly strong.

Note that we are neglecting the energy lost by the system via GWs (for further discussion on this, see Section 5).

3 TESTS

We perform a series of tests to check that our tool for the derivation of the quadrupole radiation works properly, in a similar manner to those in Lorén-Aguilar et al. (2005).

First, we simulate an isolated star and we derive numerically

³ This direction can be different from the one of spin axis. For further details see the final part of Section 4.

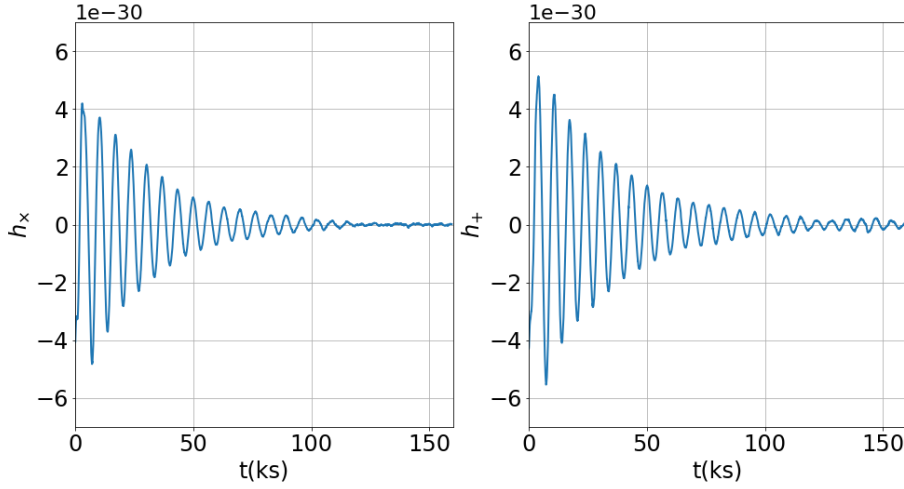


Figure 2. GW polarization amplitudes by an isolated Sun-like star at a distance of $d = 20\text{Mpc}$, plotted with respect to time (in kiloseconds). **Left:** \times polarization. **Right:** $+$ polarization.

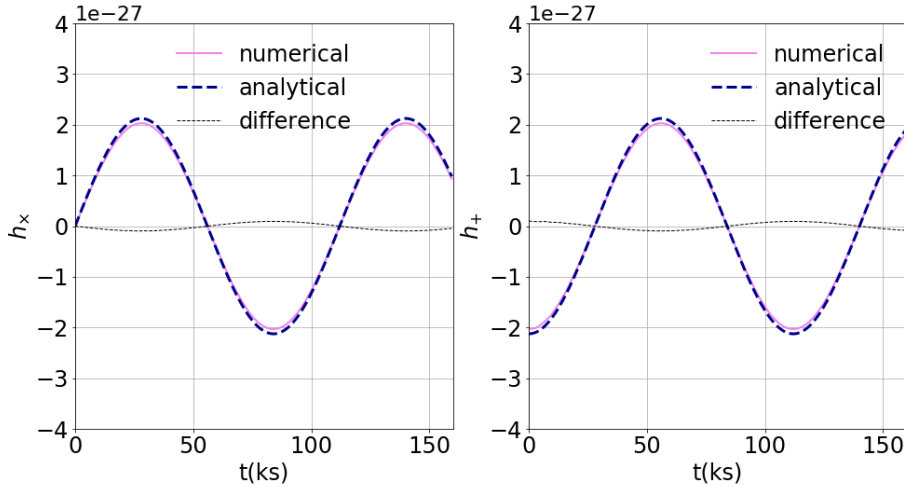


Figure 3. GW polarization amplitudes by a binary system of two Sun-like stars, separated by $R = 10R_{\odot}$, at a distance of $d = 20\text{Mpc}$ from us, plotted with respect to the time (in kiloseconds). **Left:** \times polarization seen face-on. **Right:** $+$ polarization seen face-on. The pink line is the signal calculated during the simulation, while the blue dashed-line represents the analytical solution assuming point sources. The black dashed line is the difference between the numerical and the analytical curves.

its GW emission. Theoretically we expect the signal to be zero since the star is spherical and not moving. Yet this needs to be verified because SPH particles are not initially in equilibrium. We simulate a Sun-like star, assumed to be a polytropic sphere with index $\gamma = 5/3$, at a distance of 20Mpc from us, using $\approx 10^4$ equal-mass particles. Our results are illustrated in Figure 2. On the left we show the \times polarization, on the right the $+$ polarization. Amplitudes are plotted with respect to time, expressed in kiloseconds. While the star is reaching equilibrium ($t < 100$ ks), the GW emission produced by SPH particles decreases rapidly. After the equilibrium ($t > 100$ ks), the emission has become at least one order of magnitude lower ($\sim 10^{-31}$). We can consider this residual emission due to SPH particles oscillations negligible, since much smaller than any signals produced by astrophysical sources of interest located at the same distance. For instance, in the case of a TDE of a Sun-like star

disrupted by a $10^6 M_{\odot}$ BH at 20 Mpc, this residual emission is 9 orders of magnitude lower than the GW burst associated to the disruption.

Second, we investigate the emission associated with a stellar binary, assuming Newtonian gravity in Minkowski metric plus small perturbations. We assume two stars of mass M_1 and M_2 , separated by R , moving on a circular orbit with angular velocity ω at a distance d from the observer. The GW emission is (see, e.g., [Maggiore 2007](#))

$$h_{\times}(t, d, \eta) = \frac{4G\mu\omega^2 R^2}{dc^4} \cos\eta \sin(2\omega t), \quad (7)$$

$$h_{+}(t, d, \eta) = \frac{4G\mu\omega^2 R^2}{dc^4} \left(\frac{1 + \cos^2\eta}{2} \right) \cos(2\omega t), \quad (8)$$

where $\mu = M_1 M_2 / (M_1 + M_2)$ is the reduced mass of the system. For this scenario, we consider two Sun-like stars separated by $10R_{\odot}$,

each simulated as a polytropic sphere with $\gamma = 5/3$ and 10^4 equal-mass particles. The system is located at a distance $d = 20$ Mpc. After relaxing the system, we let the simulation evolve for ≈ 1 orbit. Figure 3 shows the emission with respect to time (in kiloseconds). In pink we show the signal derived with GRPHANTOM during the simulation, while the analytical solution is illustrated with the blue dashed-line. The layout of the panels is the same as in the previous figure. The plots show agreement to within $\approx 4\%$ between the numerical and the analytical solution.

4 GRAVITATIONAL WAVES FROM TIDAL DISRUPTION EVENTS

4.1 Physical properties of tidal disruption events

The standard picture of a TDE (see, e.g., Rees 1988, Phinney 1989) considers a star with mass $M_* = m_* M_\odot$ and radius $R_* = r_* R_\odot$, on a Keplerian orbit around a massive BH $M_h = m_h M_\odot$ (M_\odot and R_\odot are the mass and the radius of the Sun respectively). The star is torn apart by BH tides if the stellar pericenter r_p falls in the range $r_s \lesssim r_p \lesssim r_t$. Here r_t is the tidal radius, that is the distance where BH tides equal the stellar self-gravity,

$$r_t \approx \left(\frac{M_h}{M_*}\right)^{1/3} \approx 7 \times 10^{10} \left(\frac{m_h}{m_*}\right)^{1/3} r_* \text{ cm}, \quad (9)$$

and r_s is the BH Schwarzschild radius

$$r_s = \frac{2GM_h}{c^2} \approx 3m_h \times 10^5 \text{ cm}. \quad (10)$$

The strength of the event is quantified by the penetration factor $\beta = r_t/r_p$. Following the previous considerations, β spans the following interval

$$1 \lesssim \beta \lesssim \beta_{\max} = \frac{r_t}{r_s} = 2 \times 10^5 r_* m_h^{-2/3}. \quad (11)$$

After the disruption, roughly half of the stellar debris falls back at the pericenter and emits luminous X-ray flares (see, e.g., Rees 1988 and Evans & Kochanek 1989). Then, the debris circularize and form an accretion disc (see, e.g., Bonnerot & Stone 2021). To date, around ~ 20 robust X-ray TDEs have been observed (see the review by Saxton et al. 2020 and references therein). Another ~ 30 TDEs have been detected in the optical (see the review by van Velzen et al. 2020 and references therein). Few of them present both X-ray and optical radiation, but the majority seem to be part of a different electromagnetic class of TDEs. The mechanism behind this kind of emission is still theoretically debated (see, e.g., Lodato & Rossi 2011, Roth et al. 2020, Bonnerot & Stone 2021). Thanks to future surveys and a growing number of electromagnetically detected TDEs it will be possible to collect more information and solve this problem.

TDEs also emit GWs. In particular we can distinguish between i) GW burst emitted when the star is torn apart at r_p (variation of the mass quadrupole of the BH-star system; see, e.g., Kobayashi et al. 2004), ii) GW production when the star is stretched and compressed by BH tides while approaching the pericenter (variation of the internal mass quadrupole of the star; see, e.g., Guillochon et al. 2009 and Stone et al. 2013) and iii) GW radiation at later stages (see, e.g., Kiuchi et al. 2011 and Toscani et al. 2019 for emission after the circularization). Focusing on i), that for standard values of the parameters involved in the disruption is the strongest contribute to the GW emission, we have that the GW amplitude, h , and the

duration of the signal, τ , can be estimated as (see, e.g., Kobayashi et al. 2004, Toscani et al. 2020)

$$h \approx \beta \times \frac{m_*^{4/3} m_h^{2/3}}{d_{20} r_*} \times 2 \times 10^{-26}, \quad (12)$$

$$\tau \approx \beta^{-3/2} \times m_*^{-1/2} r_*^{3/2} \times 10^4 \text{ s}, \quad (13)$$

where d_{20} is the distance in units of 20 Mpc.

4.2 Tidal disruption events with GR-PHANTOM

We first simulate the TDE of a main sequence (MS) star of $1M_\odot$ and $1R_\odot$ on a parabolic orbit around a non-rotating BH $M_h = 10^6 M_\odot$, with $\beta = 1$, in order to compare our results with the same case presented in Kobayashi et al. 2004. We assume a source located at a distance of 20 Mpc and we simulate a polytropic $\gamma = 5/3$ sphere with 10^5 equal-mass particles. Some snapshots of this simulation are illustrated in Figure 4.

The GW signal is plotted in Figure 5, with respect to time (in kiloseconds), where we show the waveforms $h_+(t)$, $h_\times(t)$ and also the GW strain approximated as root-square-sum amplitude $|h(t)| = \sqrt{|h_+(t)|^2 + |h_\times(t)|^2}$. First, we note that the maximum value of the signal is $\approx 3 \times 10^{-22}$, while the duration ≈ 10 ks, both values being consistent with equations (12) and (13) respectively. These results are also consistent with the plot in the top panel of Figure 5 by Kobayashi et al. 2004.⁴

4.2.1 Resolution check

We perform a resolution test to see how many particles we need to reproduce the signal illustrated in Figure 5. Thus, we repeat the same simulation with 10^4 , 10^5 , 5×10^5 and 10^6 particles. As shown in figure 6, 10^4 particles are already enough to obtain the desired curve, indicating that GWs are only sensitive to the bulk mass distribution. In addition to this, we have also calculated the relative differences between the curves, to be sure about the convergence. We see that the absolute errors are of order $\sim 10^{-4}$, thus confirming the convergence.

4.3 TDE gravitational catalogue

In this Section we present the simulation included in our atlas and the parameter space explored. The catalogue is available online at <https://gwcataloguetdes.fisica.unimi.it>.

Orbital inclination. In the GW catalogue we assume that the stellar orbit lies in the $\mathbf{x} - \mathbf{y}$ plane (see geometry in Figure 1). In practice, in GRPHANTOM, in the case of a spinning BH, the coordinate choice naturally has the \mathbf{z} axis pointing in the BH spin direction. In these cases, we then simulate an encounter with an inclined stellar orbit with respect to the \mathbf{z} axis, by the desired angle θ , and then rotate the results back into the $\mathbf{x} - \mathbf{y}$ plane *before computing* the GW emission.

TDE of a Sun-like star. We consider a Sun-like star on an orbit with three possible inclination angles with respect to the BH spin: $\theta = 0 - 30^\circ - 60^\circ$. For each value of this angle, we span the BH mass over the following values: $m_h = 10^5 - 10^6 - 10^7$. Each BH has three

⁴ There is a minus sign of difference between our plot of h_+ and the one presented in Kobayashi et al. 2004, probably due to a π difference in the viewing angle.

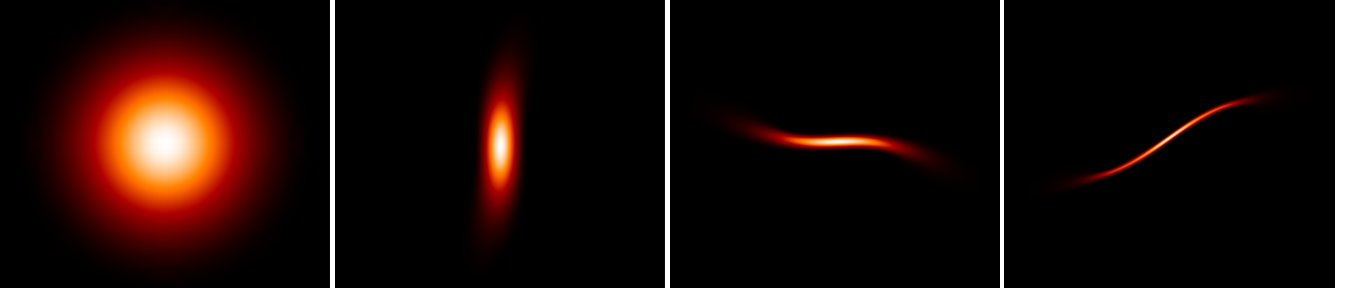


Figure 4. Surface density plots for the TDE simulation described in Section 4.2. From left to right: star at the beginning of the simulation (first panel), during the disruption (second panel), leaving the pericenter (third and fourth panel). These snapshots are generated with SPLASH (Price 2007), an SPH visualization code.

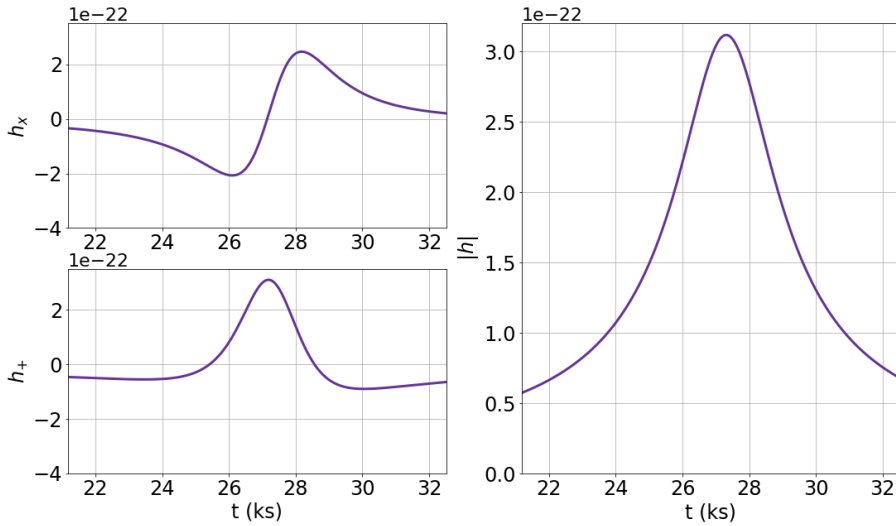


Figure 5. GW emission from a TDE of a MS star with $M_* = 1M_\odot$ and $R_* = 1R_\odot$ on a parabolic orbit around a Schwarzschild BH with $M_h = 10^6 M_\odot$, plotted with respect to time (in kiloseconds). The penetration factor is $\beta = 1$ and the source is at $d = 20\text{Mpc}$. **Top left:** \times polarization seen face-on. **Bottom left:** $+$ polarization seen face-on. **Right:** Root-square-sum amplitude.

possible values of the spin: $a = 0 - 0.5 - 0.9$. For every scenario we consider both elliptical orbits (with eccentricities $e=0.6, e=0.8$) and parabolic ($e=1$). All orbits are prograde. For $m_h = 10^7$ we limit to $\beta = 1$ (because for higher penetrations the star is swallowed whole before disruption), while for the other BH masses we consider three values of β : 1-2-5. Additionally, for $m_h = 10^6$ we have decided to investigate also the retrograde scenario ($\theta = 180$) with values of the β parameters equal equal to 1 and 2.

Overall, we have performed 207 simulations. If we remove those with spinless BH and different θ , that are equivalent to each other thanks to spherical symmetry, the effective number of simulations is 147.

TDE of a MS star. We consider a MS star with $M_* = 10M_\odot$, with a radius in solar units (see Kippenhahn & Weigert 1990)

$$r_* = m_*^{0.57} \approx 3.7. \quad (14)$$

We assume the star to be disrupted by a $10^7 M_\odot$ BH, with spin $a = 0 - 0.5 - 0.9$. We examine three values of the eccentricities $e = 0.6 - 0.8 - 1$ and we keep the penetration factor fixed to 1. All the orbits are prograde. The inclination angles are

$\theta = 0 - 30^\circ - 60^\circ$. Overall, we have performed 27 simulations. Due to the spherical symmetry, the effective number of simulations is 21.

TDE of a WD. We consider a WD star of mass $0.5M_\odot$ and radius $10^{-2}R_\odot$ (see Shapiro & Teukolsky 1983) disrupted by a $10^4 M_\odot$ BH, with spin $a = 0 - 0.5 - 0.9$. We investigate three values of the eccentricities $e = 0.6 - 0.8 - 1$ and we take $\theta = 0$. The penetration factor is fixed to 1. Since the stellar mass is far from the Chandrasekar limit, we can simulate the star as a polytrope with $\gamma = 5/3$ instead of $\gamma = 4/3$. Overall, we have performed 9 simulations.

At the time of writing, our online catalogue contains a total number of waveforms equals to 243. However, we consider this a *live* catalogue and our plan is to continue to expand it over time, in order to cover more parameter space and make it as comprehensive as possible.

Distance and orientation of the events In our catalogue, the star is always assumed to lie at a distance of 1 Mpc. The user can easily rescale the results to any assumed distance. Also, for each simulation

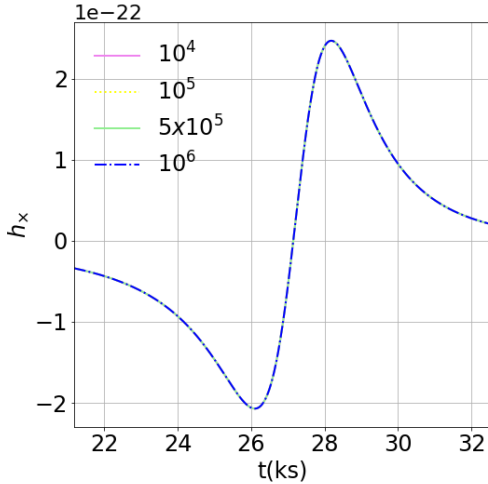


Figure 6. GW signal for a TDE of a Sun-like star, as described in figure 5. We plot the \times polarization with respect to the time (in kiloseconds) for 10^4 , 10^5 , 5×10^5 and 10^6 particles. All the curves obtained coincide.

the catalogue includes the GW emission computed assuming the following values of the angles (η, ϕ) : $(0, 0)$, $(30, 0)$, $(60, 0)$, $(90, 0)$. However, we also offer the components of the second time derivative of the moment of inertia, so the user can compute easily the GW signal with any geometry, by using equation (1).

5 DISCUSSION

Here we discuss some of the results from our simulations. The distance of the source is fixed at 20 Mpc and the polytropic index is $\gamma = 5/3$. All the calculations are performed in Kerr metric expressed with Boyer-Lindquist coordinates. The transformations from code to physical units are given by

$$t_{\text{phys}} = 4.96 \text{ s} \times t_{\text{code}} \times \left(\frac{M_{\text{h}}}{10^6 M_{\odot}} \right), \quad (15)$$

$$l_{\text{phys}} = 0.0098 \text{ au} \times l_{\text{code}} \times \left(\frac{M_{\text{h}}}{10^6 M_{\odot}} \right), \quad (16)$$

$$M_{\text{phys}} = M_{\text{code}} \times M_{\text{h}}, \quad (17)$$

where t , l and M stand for time, length and mass respectively.

5.1 Changing the physical parameters

5.1.1 Spin

First, we have investigated if the spin affects the GW signal, considering prograde orbits with respect to the spin of the BH. We have found that, if compared to the static BH scenario, i) the spin changes the shapes of the polarization amplitudes during and after the passage at the pericenter, shifting the peak of the waveforms at later times and lowering it, ii) the peak of the root-square-sum decreases while the spin increases.

In Figure 7, we illustrate a close orbit in the $\mathbf{x} - \mathbf{y}$ plane with eccentricity $e = 0.6$ and penetration factor $\beta = 5$. We plot the polarizations \times (top left) and $+$ (bottom left) seen face-on and the related root-square-sum amplitude $|h|$, versus time (in kiloseconds). In each panel we consider three values for the spin: $a = 0$ (blue), $a = 0.5$

(green) and $a = 0.9$ (pink). Deviations from the static BH case are clearly visible in each plot, starting from ≈ 1.8 ks, that corresponds to the star passing through r_{p} . The peak in the strain for $a = 0.9$ is smaller than the peak for spinless BH by a factor ≈ 1.4 .

In Figure 8, we plot $|h|_{\text{max}}$ for the same scenario as before but as a function of β . We can see that h_{max} starts to be affected by the spin already at low β (≈ 2), even though the spin effect can be appreciated more easily at $\beta \approx 5$. Thus, the proportionality between the maximum value of the GW signal and β predicted from theory (cf. 12), seems to hold. For the case of rotating BHs the proportionality constant is ≈ 1 as expected, while for the spinless case this constant seems to be between $1 \sim 2$.

Contrary, for retrograde orbits ($\theta = 180^\circ$) we see the GW signal increases for higher values of a . In Figure 9, we plot $|h|$ versus time (in kiloseconds), for a Sun-like star disrupted by a $10^6 M_{\odot}$ BH. The penetration factor is equal 2 and the eccentricity is 0.6. We consider three different values of the BH spin: $a = 0$ (blue), $a = 0.5$ (green) and $a = 0.9$ (pink). The difference between the peak corresponding to $a = 0.9$ BH respect to the spinless BH is roughly 6%. From our results, it seems that GW amplitudes are stronger for high spin retrograde orbits and weaker for high spin prograde orbits. We interpret this result as due to the higher angular frequency that a retrograde orbiter experiences. In fact, the orbital frequency of a test particle orbiting around a spinning BH is (Bardeen et al. 1972)

$$|\nu_{\phi}| = \frac{c^3}{2\pi G M_{\text{h}}} \left| \frac{1}{(2r/r_{\text{g}})^{3/2} \pm a} \right|. \quad (18)$$

From the above equation we see that the angular frequency increases for higher retrograde (-) BH spins.

5.2 Changing the orbital parameters

5.2.1 Inclination angle

If the central BH is not rotating, the GWs should be independent of the orbital inclination θ , thanks to the spherical symmetry of the system. The results of our simulations proved this assumption i) both in the case of spinless BH and ii) for star far enough from the BH so that the effects of rotation are negligible. Contrarily, when the spin *does* modify the shape of the signal, the condition of spherical symmetry does not hold anymore and thus different values of θ change the signal emitted by the TDE.

In Figure 10, we illustrate the GW polarization amplitudes for a close orbit ($e = 0.8$) of a Sun-like star disrupted by a $10^6 M_{\odot}$ BH. We plot the \times polarization seen face-on for $\beta = 1$ with spinless BH (top left) and spin $a = 0.9$ (bottom left) and for $\beta = 5$ with spinless BH (top right) and spin $a = 0.9$ (bottom right). The black curve refers to $\theta = 0$, the grey for $\theta = 30^\circ$ and the brown for $\theta = 60^\circ$. We see that the values of θ have an effect on the amplitudes only in the panel on the lower right, where the changes are appreciable during and following the passage at the pericenter (cf. paragraph 5.1.1). As for the strain, the peak slightly decreases together with the inclination angles ($\approx 7\%$), as illustrated in Figure 11.

5.2.2 Eccentricity

An additional orbital parameter that can have an impact on the GW signal emitted by tidally disrupted stars is the geometry of the orbit. We consider three values of the eccentricity: $e = 0.6$ and $e = 0.8$ for elliptical orbits and $e = 1$ for parabolic orbits. From the numerical outputs of our simulations, we find that different values of the eccentricities modify the polarization amplitudes both *before*

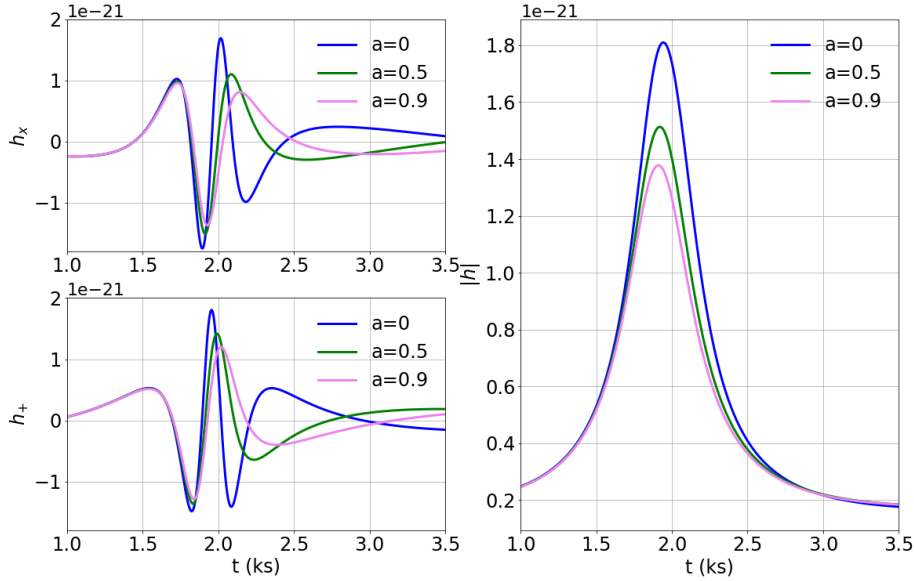


Figure 7. Sun-like star disrupted by a $10^6 M_\odot$ BH. The orbital inclination is $\theta = 0$, the penetration factor is $\beta = 5$ and the eccentricity $e = 0.6$. Prograde orbits. **Top left:** \times polarization seen face-on. **Bottom left:** $+$ polarization seen face-on. **Right:** Related root-square-sum amplitude. All the curves are plotted with respect to time (in kiloseconds). The three colours stand for three different BH spin values: blue $a = 0$, green $a = 0.5$ and pink $a = 0.9$. We can see that increasing the spin changes the shapes of the polarization amplitudes during and after the pericenter, shifting the peak of the waveforms at later times and lowering it, and that the peak of the root-sum-square amplitude decreases while the spin increases. The peak for $a = 0.9$ is a factor 1.4 smaller than the peak for spinless BH.

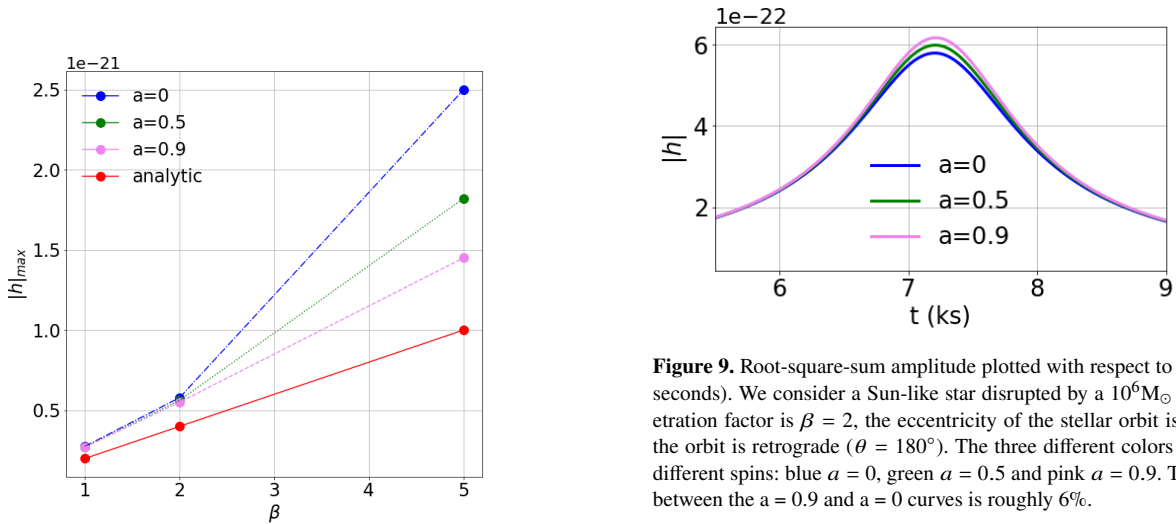


Figure 8. Maximum root-square-sum amplitude versus β for a Sun-like star disrupted by a $10^6 M_\odot$ BH. The orbital inclination is $\theta = 0$, the eccentricity $e = 0.6$, prograde orbits. The three different colours stand for three different BH spins: blue $a = 0$, green $a = 0.5$ and pink $a = 0.9$. The red solid line shows the linear relationship between the penetration factor and the maximum GW amplitude predicted from Equation (12). This line is lower than the others since the GW amplitude increases for higher values of the eccentricity, while Equation (12) refers to null eccentricity (cf. paragraph 5.2.2).

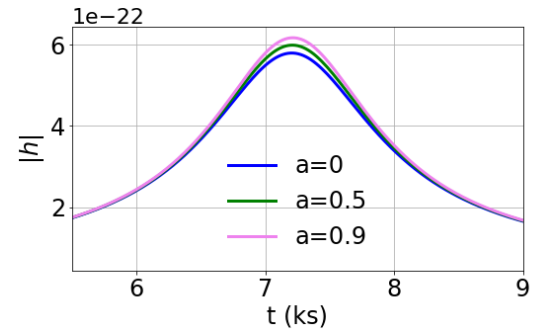


Figure 9. Root-square-sum amplitude plotted with respect to time (in kiloseconds). We consider a Sun-like star disrupted by a $10^6 M_\odot$ BH; the penetration factor is $\beta = 2$, the eccentricity of the stellar orbit is $e = 0.6$ and the orbit is retrograde ($\theta = 180^\circ$). The three different colors refer to three different spins: blue $a = 0$, green $a = 0.5$ and pink $a = 0.9$. The difference between the $a = 0.9$ and $a = 0$ curves is roughly 6%.

and *after* the passage at the pericenter. As for the strain, the peak increases with the eccentricity. This can be explained as followed. The GW burst from TDEs is produced around the pericenter, when the star is torn apart by the BH tides. At the pericenter, assuming Keplerian velocity, v_{kepl} reads

$$v_{\text{kepl}} = \left[\frac{GM_{\text{h}}}{r_{\text{p}}} (1+e) \right]^{1/2} \propto (1+e)^{1/2}. \quad (19)$$

We see that for higher eccentricities the star goes through the pericenter faster. This results in a stronger gravitational signal.

In Figure 12, we illustrate the scenario of a Sun-like star disrupted by a $10^6 M_\odot$ spinless BH, with $\beta = 1$. We can see that the

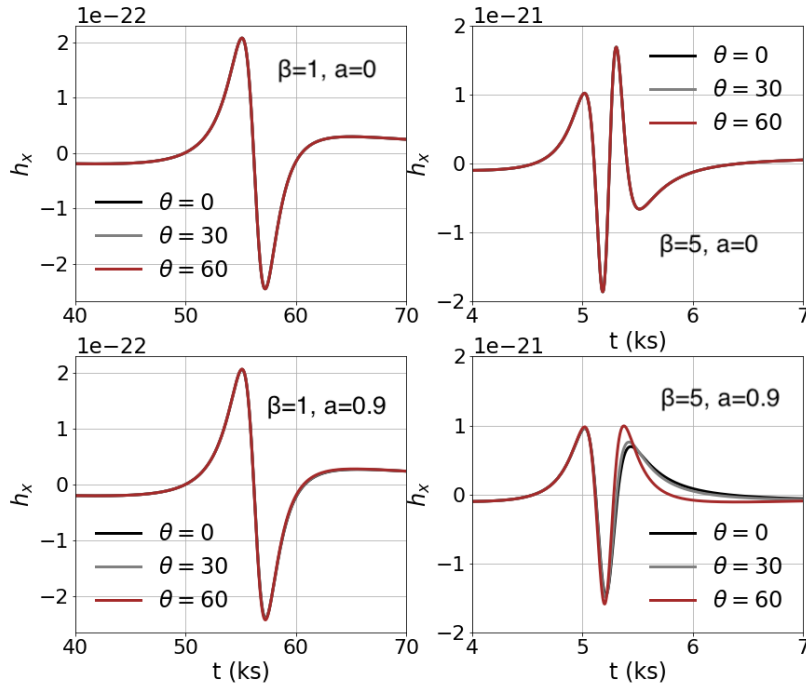


Figure 10. Sun-like star disrupted by a $M_h = 10^6 M_\odot$ BH. Eccentricity $e=0.8$, prograde orbits. **Top left:** \times polarization seen face-on. $\beta = 1$, spinless BH. **Bottom left:** \times polarization seen face-on. $\beta = 1$, $a = 0.9$. **Top right:** \times polarization seen face-on. $\beta = 5$, $a = 0$. **Bottom right:** \times polarization seen face-on. $\beta = 5$, $a = 0.9$. All the curves are plotted with respect to time (in kiloseconds). The black curve stands for $\theta = 0$, the grey for $\theta = 30^\circ$ and the brown for $\theta = 60^\circ$. From this Figure, it is possible to see that different inclination angles of the stellar orbits affect the GW emission only when we have both high values of β and high BH spins.

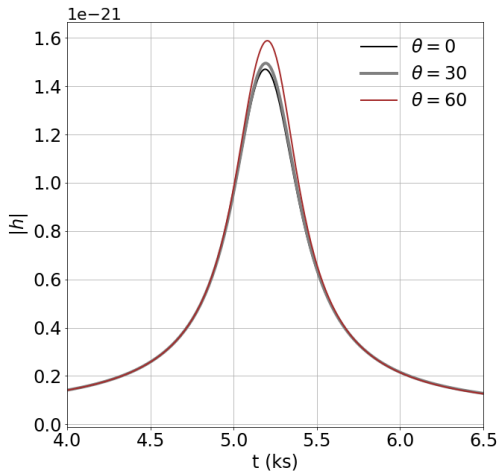


Figure 11. Root-square-sum signal plotted with respect to time (in kiloseconds) for the same scenario as the one illustrated in the right panel of Figure 10. The peak decreases together with the inclination angles ($\approx 7\%$).

differences in the polarization amplitudes for each eccentricity are well visible. As for the strain, the black dashed line represent the analytical estimates, that is a factor 1.5 lower than the peak for the parabolic trajectory ($(1+e)^{1/2} = 2^{1/2} \approx 1.4$) consistent with our

estimates of Equation (12), since the analytical estimates assumes a circular orbit ($e \approx 0$).

5.3 Return to pericenter

We have investigated if the debris, falling back to the pericenter, produce a GW signal comparable to the one emitted when the star is torn apart. We consider a Sun-like star disrupted by a static $10^6 M_\odot$, on a close orbit ($e = 0.8$) in the $x - y$ plane with $\beta = 1$. We evolve the simulation for ~ 3 orbits. From Figure 13, we can see that, when the debris falls back to r_p for the first time ($t \approx 170$ ks), they produce a bump in the strain, that is a factor ≈ 10 smaller than the disruption signal. For the following passages at the pericenter, the gravitational contribution is even lower (see Toscani et al. 2019 for further discussion on this secondary emission).

It would be interesting if this second bump could be seen by future interferometers. Indeed, when we talk about the multimessenger prospects for TDEs, we think to detect the GW signal from the disruption followed after some days by the electromagnetic counterpart. But, if this second bump could be revealed, the electromagnetic signal would be accompanied by GW detection and thus we would be able to collect more and complementary information on the circularization process and possibly on the emission mechanism that fuel TDE flares.

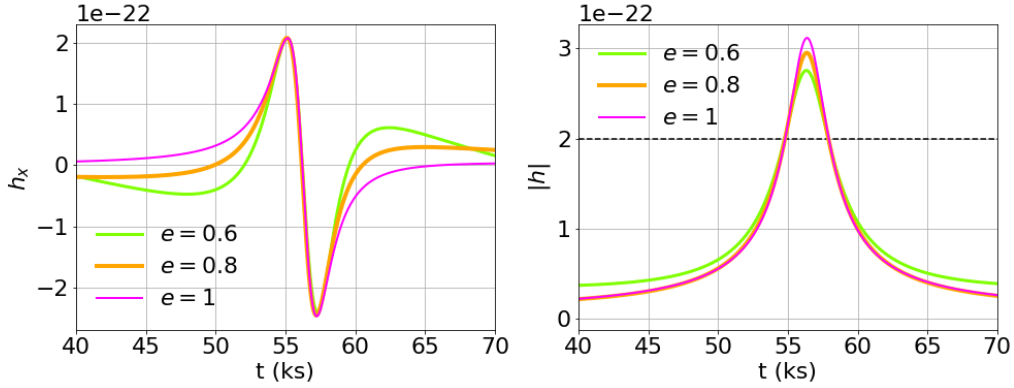


Figure 12. Sun-like star disrupted by a $M_h = 10^6 M_\odot$ spinless SMBH. The orbital inclination is $\theta = 0$, the penetration factor is $\beta = 1$. **Left:** \times polarization seen face-on. **Right:** related strain. All the curves are plotted with respect to time (in kiloseconds). The light green curve refers to $e = 0.6$, the orange to $e = 0.8$ and the magenta to $e = 1$. The black horizontal dashed line is the analytical estimate of the strain (see equation 12).

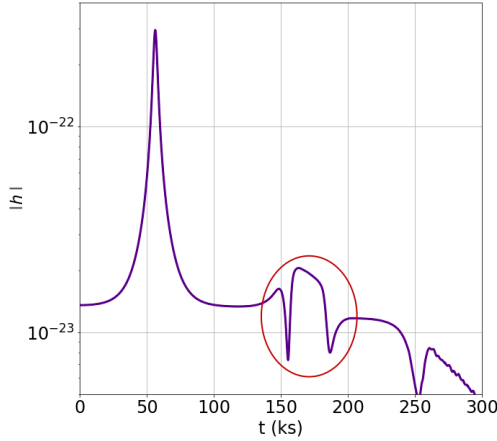


Figure 13. GW signal produced by a Sun-like star disrupted by a Schwarzschild BH with mass $M_h = 10^6 M_\odot$ BH. The orbital inclination is $\theta = 0$, the penetration factor is $\beta = 1$, the eccentricity $e = 0.8$. During the first passage at the pericenter (≈ 70 ks) the star is torn apart by the BH tides and the first GW burst is produced. Then the debris starts the circularization process around the BH. Here we consider ~ 2 returns to the pericenter. With the red circle we outline the bump in the strain due to the first return r_p .

5.3.1 Energy lost by GW emission

In the previous example we should have considered the energy lost by the system via GWs, E_{gw} , to be sure that the orbit done by the debris is the correct one. Yet, we expect E_{gw} to be small enough relative to the orbital energy of the star and so negligible. Here we present a quick way to estimate this quantity.

If we consider a Sun-like star disrupted by a $10^6 M_\odot$ BH with $\beta = 1$, the third derivative of the moment of inertia of the system can be approximated as

$$\ddot{M} \approx \frac{M_* r_t^2}{\tau^3}. \quad (20)$$

In the above Equation we have assumed the star as a point-mass particle orbiting around the BH at a distance of r_t . Thus, we have calculated the moment of inertia of the system as $M r_t^2$ and we have derived its third derivative with respect to time dividing it by the cube of the period, τ^3 . Consequently, the luminosity associated with

the GW burst is

$$L_{\text{gw}} \approx \frac{G}{5c^5} \left[M_* r_t^2 \left(\frac{1}{\tau} \right)^3 \right]^2. \quad (21)$$

As a result, the energy lost by the system over a period will be approximately $E_{\text{gw}} \approx 10^{37}$ erg. The absolute value of the orbital energy for the same system reads

$$E_{\text{orb}} = \frac{G M_h M_*}{2r_t} \approx 10^{52} \text{ erg}. \quad (22)$$

Thus we see that E_{gw} is fifteen orders of magnitude lower than the orbital energy of the system and, consequently, it is safe to neglect the back-reaction of the GW emission.

5.4 Angular distribution of quadrupole radiation

We recall that η is the angle between the los and the normal to the orbit, while ϕ is the angle between the projection of the line of sight on the $\mathbf{x} - \mathbf{y}$ plane and the pericenter.⁵

5.4.1 Changing η

We have investigated what happens if we consider $\phi = 0$ and we change η . Figure 14 shows the \times polarization (left) and the strain (right) with respect to the time (in kiloseconds). We consider the observer along the normal to the orbit (blue curve), inclined by 30° (orange curve) and by 60° (green curve) respect to the \mathbf{z} axis. The strain is strongest when the observer see the signal face-on. As we could expect, the signal is strongest when it propagates along the direction of the line of sight, otherwise it decreases.

5.4.2 Changing ϕ

We have investigated what happens if we consider $\eta = 30^\circ$ and we change ϕ . We can see from Figure 15 that if the projection of the los moves away from the pericenter sight, the signal decreases.

⁵ So far we have kept this angle fixed to 0, in the same way we present the waveforms in the catalogue.

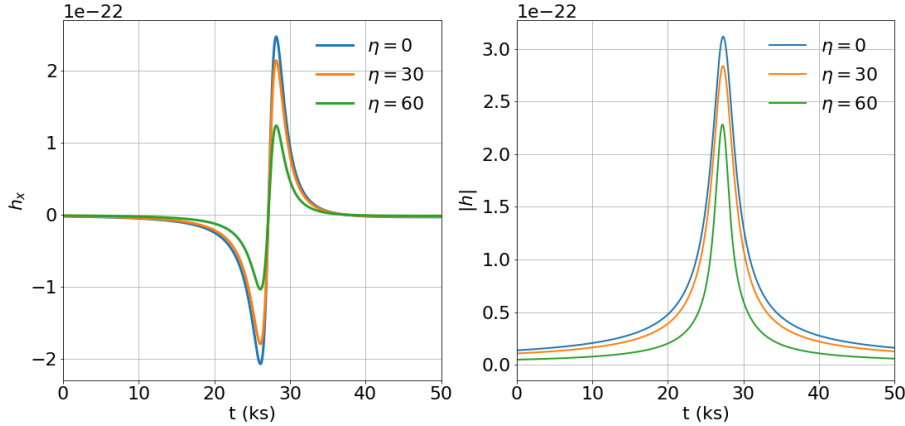


Figure 14. Sun-like star disrupted by a $10^6 M_{\odot}$ spinless SMBH. The orbital inclination is zero, the penetration factor is $\beta = 1$. **Left:** \times polarization. **Right:** related strain. All the curves are plotted with respect to time (in kiloseconds). The blue curve refers to $\eta = 0$, the orange to $\eta = 30^\circ$ and the green to $\eta = 60^\circ$.

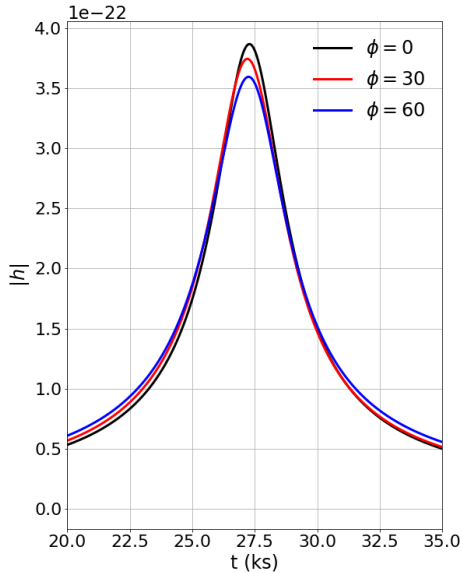


Figure 15. Sun-like star disrupted by a $10^6 M_{\odot}$ spinless SMBH. We have $\eta = 30^\circ$, while the penetration factor is $\beta = 1$. Root-square-sum amplitude plotted with respect to time (in kiloseconds). The black curve is for $\phi = 0$, while the blue curve for $\phi = 60^\circ$. All the curves are plotted with respect to time (in kiloseconds).

6 CONCLUSIONS

In this paper, we have implemented a new method for the derivation of GWs in `GRPHANTOM`, an SPH code including GR dynamics. Our tool is based on the discretization of the second time derivative of the moment of inertia and then the GWs are calculated in the weak field approximation. We test it for some well-known systems (isolated star, binary far from the merger phase). Then, we use it to derive the GW emission from TDEs, spanning the space of parameters. The main results we have obtained from the simulations are the following:

(i) the spin affects the GW polarization amplitudes during and after the passage at the pericenter. The strain decreases with the increasing of the spin for prograde orbits, while the opposite occurs for retrograde orbits;

(ii) the orbital inclination affects the GW emission from TDEs only if the BH is spinning and the star is close enough to feel the effect of the spin;

(iii) different eccentricities modify the polarization amplitudes. The strain increases for higher eccentricities, due to the fact that the velocity at pericenter is $\propto (1 + e)^{1/2}$;

(iv) after the disruption, the debris falling back at the pericenter produces a bump in the strain ~ 1 order of magnitude lower than the signal at the pericenter;

(v) the GW emission is stronger if we observe the system face on and if the signal is along the axis of the pericenter.

From these results, it seems likely that TDEs discovered through GWs will be biased towards face-on low-spin prograde TDEs/high-spin retrograde TDEs, with very eccentric orbits.

All the results of the simulations can be found online at the following <https://gwcataloguetdes.fisica.unimi.it>. We believe that such a catalogue can be a useful resource of templates to easily classify the GW emission from TDEs once this kind of signal will be able to be detected by future interferometers.

ACKNOWLEDGMENTS

This project has received funding from the European Union’s Horizon 2020 research and innovation program under the Marie Skłodowska-Curie grant agreement NO 823823 (RISE DUST-BUSTERS project). We acknowledge CPU time on OzSTAR, funded by Swinburne University and the Australian Government.

DATA AVAILABILITY STATEMENT

The data underlying this article are available at <https://gwcataloguetdes.fisica.unimi.it>, and can be accessed freely by any user.

REFERENCES

Abbott B. P., et al., 2017, *Phys. Rev. Lett.*, 19, 161101
 Abell P. A., et al., 2009, LSST Science Book, Version 2.0, <https://arxiv.org/abs/0912.0201>

- Alexander K. D., van Velzen S., Horesh A., Zauderer B. A., 2020, *Space Sci. Rev.*, 216, 81
- Amaro-Seoane P., et al., 2017, Laser Interferometer Space Antenna, <http://arxiv.org/abs/1702.00786>
- Barcons X., et al., 2012, Athena (Advanced Telescope for High ENergy Astrophysics) Assessment Study Report for ESA Cosmic Vision 2015-2025, <https://arxiv.org/abs/1207.2745>
- Bardeen J. M., Press W. H., Teukolsky S. A., 1972, *ApJ*, 178, 347
- Bonnerot C., Stone N. C., 2021, *Space Sci. Rev.*, 217, 16
- Buonanno A., 2007, Gravitational waves, <http://arxiv.org/abs/0709.4682>
- Einstein A., 1918, Sitzungsberichte der Königlich Preußischen Akademie der Wissenschaften (Berlin), Seite 154-167.
- Evans C. R., Kochanek C. S., 1989, *ApJ*, 346, L13
- Gaskin J. A., et al., 2018, Space Telescopes and Instrumentation 2018: Ultraviolet to Gamma Ray. den Herder, Jan-Willem A. and Nikzad, Shouleh and Nakazawa, Kazuhiro
- Gingold R. A., Monaghan J. J., 1977, *MNRAS*, 181, 375
- Goldstein A., et al., 2017, *ApJ*, 848, L14
- Guillochon J., Ramirez-Ruiz E., Rosswog S., Kasen D., 2009, *ApJ*, 705, 844
- Kippenhahn R., Weigert A., 1990, Stellar Structure and Evolution. <https://ui.adsabs.harvard.edu/abs/1990sse.book.....K>, <https://ui.adsabs.harvard.edu/abs/1990sse.book.....K>
- Kiuchi K., Shibata M., Montero P. J., Font J. A., 2011, *Phys. Rev. Lett.*, 106, 251102
- Kobayashi S., Laguna P., Phinney E. S., Meszaros P., 2004, *ApJ*, 615, 855
- Liptai D., Price D. J., 2019, *MNRAS*, 485, 819
- Lodato G., Rossi E. M., 2011, *MNRAS*, 40, 359
- Lodato G., Cheng R. M., Bonnerot C., Dai J. L., 2020, *Space Sci. Rev.*, 216, 63
- Lorén-Aguilar P., Guerrero J., Isern J., Lobo J. A., García-Berro E., 2005, *MNRAS*, 356, 627
- Lucy L. B., 1977, *Astronomical Journal*, 82, 1013
- Luo J., et al., 2016, *Classical and Quantum Gravity*, 33, 035010
- Maggiore M., 2007, Gravitational Waves. Volume 1: Theory and Experiments. Oxford University Press, doi:10.1007/s10714-009-0762-5
- Pfister H., Toscani M., Wong T. H. T., Lixin Dai J., Lodato G., Rossi E. M., 2021, Observable gravitational waves from tidal disruption events and their electromagnetic counterpart, <https://arxiv.org/abs/2103.05883>
- Phinney E. S., 1989, in Morris M., ed., IAU Symposium Vol. 136, The Center of the Galaxy, p. 543, <https://ui.adsabs.harvard.edu/abs/1989IAUS..136..543P/abstract>
- Price D. J., 2007, *Publ. Astron. Soc. Australia*, 24, 159
- Price D. J., 2012, *Journal of Computational Physics*, 231, 759
- Price D. J., et al., 2018, *Publ. Astron. Soc. Australia*, 35, e031
- Rees M. J., 1988, *Nature*, 333, 523
- Rossi E. M., Stone N. C., Law-Smith J. A. P., MacLeod M., Lodato G., Dai J. L., Mandel I., 2020, arXiv e-prints
- Rosswog S., 2009, *New Astron. Rev.*, 53, 78
- Roth N., Rossi E. M., Krolik J., Piran T., Mockler B., Kasen D., 2020, *Space Sci. Rev.*, 216, 114
- Sato S., et al., 2017, *Journal of Physics: Conference Series*, 840, 012010
- Saxton R., Komossa S., Auchettl K., Jonker P. G., 2020, *Space Sci. Rev.*, 216, 85
- Shapiro S. L., Teukolsky S. A., 1983, Black holes, white dwarfs, and neutron stars: The physics of compact objects. A Wiley-Interscience Publication, New York: Wiley, doi:10.1002/9783527617661
- Stone N., Sari R., Loeb A., 2013, *Monthly Notices of the Royal Astronomical Society*, 435, 1809
- Toscani M., Lodato G., Nealon R., 2019, *MNRAS*, 489, 699
- Toscani M., Rossi E. M., Lodato G., 2020, *MNRAS*, 498, 507
- van Velzen S., Holoien T. W. S., Onori F., Hung T., Arcavi I., 2020, *Space Sci. Rev.*, 216, 124

This paper has been typeset from a $\text{\TeX}/\text{\LaTeX}$ file prepared by the author.